Combustion and Flame 242 (2022) 112181

Contents lists available at ScienceDirect

Combustion and Flame

journal homepage: www.elsevier.com/locate/combustflame

Effects of flexoelectric and piezoelectric properties on the impact-driven ignition sensitivity of P(VDF-TrFE)/nAl films

Derek K. Messer[a,*], Ju Hwan Shin[b], Metin Örnek[a], Thomas A. Hafner[a], Min Zhou[b], Steven F. Son[a]

[a] School of Mechanical Engineering, Purdue University, West Lafayette, IN 47907, USA
[b] School of Mechanical Engineering, Georgia Institute of Technology, Atlanta, GA 30332, USA

ARTICLE INFO

Article history:
Received 6 October 2021
Revised 29 April 2022
Accepted 30 April 2022

Keywords:
Flexoelectricity
Piezoelectricity
Energetic materials
Ignition sensitivity
Aluminum, Modeling

ABSTRACT

Polyvinylidene fluoride (PVDF) and its copolymer poly(vinylidene fluoride-co-trifluoroethylene), P(VDF-TrFE), have attracted great interest due to their ability to be utilized as a matrix binder capable of producing modified ignition sensitivity in energetic systems. While there have been studies on the combustion of fluoropolymer/aluminum systems, there is still a shortage of knowledge on the role the electromechanical properties of P(VDF-TrFE) play in the processes leading to the ignition of an energetic material upon a mechanical impact. To help bridge this gap, we conducted experiment and computational simulation to elucidate the underlying flexoelectric and piezoelectric properties that P(VDF-TrFE)/nanoaluminum (nAl) films exhibit and to quantify the time duration it takes to commence ignition (i.e., ignition time). Further, multiple samples of the P(VDF-TrFE)/nAl films were used in the experiment (20 specimens per run) and the simulation (5 microstructures) with similar statistical attributes for the microstructure, allowing us to perform a probabilistic analysis on the film's ignition sensitivity. Based on our systematic assessment, we conclude that the electromechanical properties of the film, especially flexoelectricity, can influence the ignition sensitivity by locally enhancing the electric field near the nAl particles (by a factor of ~6.0) beyond the binder's breakdown strength, resulting in concentrated channels of heat dissipation and ultimately ignition reactions. The effect of poling was also investigated by comparing how the sensitivity of the poled films differs from that of the unpoled films, thereby offering a mechanism to tune the ignition sensitivity by varying the level of piezoelectricity in the films. Results indicate that poling the films can enhance the ignition sensitivity slightly by decreasing the minimum ignition energy (MIE) by 8%.

1. Introduction

Energetic materials (EM) are solids or liquids that possess a high amount of stored chemical energy that can be released via applied thermal, mechanical, optical, electrical, or other stimuli [1–3]. Common energetics include but are not limited to explosives, propellants, and pyrotechnics. Energetic materials are generally characterized by their sensitivity and reactivity. Determining the sensitivity of an EM by drop-weight impact, electrostatic discharge, friction, and thermal stability tests is crucial for robust reactivity and safety considerations [4]. Recently, there has been an increased interest in the development of smart or switchable energetic materials [5–8]. Materials that can be dialled to a specific yield or can be switched on/off are an example of this. Some efforts to develop smart energetics include electrical solid-state propellants for applications in aerospace and pyrotechnics [8].

Piezoelectric materials (e.g., ceramics or polymers with non-centrosymmetric crystallographic structure) can generate an electrical charge in response to an applied mechanical force or generate physical displacement against an applied electric field (*E*-field) [9]. Ferroelectric materials, including specific fluoropolymers, are also capable of exhibiting piezoelectricity [10,11]. Fluoropolymers have attracted great attention in the last few decades in the energetics field due to the strong oxidizing feature of fluorine (F) atoms as well as their ability to be used as binders. Fluoropolymers, such as polyvinylidene fluoride (PVDF), poly(vinylidene fluoride-co-trifluoroethylene) (P(VDF-TrFE)), polytetrafluoroethylene (PTFE), tetrafluoroethylene hexafluoropropylene vinylidene (THV), have been studied in energetic formulations [12–19]. Among these, PVDF is of particular interest because of its high fluorine content (59 wt.%) and its well-studied piezoelectric response [20–22]. PVDF is a semi-crystalline polymer that mainly exists in alpha (α),

* Corresponding author at: 500 Allison Road, West Lafayette, IN 47907.
E-mail address: messer3@purdue.edu (D.K. Messer).

https://doi.org/10.1016/j.combustflame.2022.112181
0010-2180/

beta (β), or gamma (γ) phases [23]. However, PVDF also demonstrates piezoelectric, pyroelectric, and ferroelectric properties at their strongest in the β-phase [24].

The alignment of the dipoles can be achieved through poling methods, which works when the PVDF is in the β- or γ- phase. The piezoelectric coefficient (d_{33}) characterizes the extent of the material's piezoelectricity (e.g., $d_{33} = -30$ pC/N for commercial films [25]). Post-processing methods, such as mechanical stretching, drawing, and high temperature and pressure treatments, must be performed to achieve β-phase since PVDF naturally exists in the α-phase [26]. Huang et al. demonstrated that increasing the mass fraction of β-phase PVDF by tenfold starting at 2.5% in Al-PVDF composites improves the peak pressure by 90% and the pressure rise rates by 300% [27]. This change is due to the alignment of F atoms along one side of the PVDF polymer chain in the β-phase. On the other hand, P(VDF-TrFE) is a copolymer that naturally exhibits ferroelectricity due to the formation of a more thermodynamically stable β-phase caused by the addition of TrFE [28–30]. Studies show that doping P(VDF-TrFE) with metal ZnO nanoparticles can have an influence on the phase and increase the overall piezoelectricity of the material [31,32].

Piezoelectricity is not the only source leading to the polarization of materials. Flexoelectricity can also generate electrical polarization within the materials under a strain gradient [33]. This is a major concern in energetic formulations since a spark that is possibly caused by an undesired mechanical loading may lead to an uncontrolled ignition [34]. On the other hand, flexoelectricity can also be a mechanism for tuning an EM's sensitivity. In addition to being piezoelectric, fluoropolymers, such as PVDF, are flexible, and hence, higher strain gradients can be achieved under similar stress as compared to ceramic bulk materials, resulting in strong electromechanical response [10,35]. The flexoelectric coefficients of PVDF-based materials are reported to vary up to $\sim 10^{-5}$C/m [36–39].

Among the commonly used metal fuels in energetic systems, Al has a high energy density (31 kJ/g), low density (2.7 g/cm^3) and provides a high combustion enthalpy [40,41]. Aluminum particles are coated with a passivating oxide layer (Al_2O_3, or aluminum oxide) when exposed to ambient atmosphere or oxidizing agents, and when this coating is destroyed, the aluminum ignites in an oxidizing atmosphere. Aluminum nanoparticles (nAl) has a high specific surface area, which augments its reactivity. The fluorination of Al releases greater energy than its reaction with oxygen as shown by the reaction of Al with polytetrafluoroethylene (PTFE) generating 21 GJ/m^3, whereas the best molecular explosives generate less than 12 GJ/m^3 [42]. A pre-ignition reaction (PIR) can be used to describe the exothermic surface reaction that occurs before the main nAl oxidation reaction. PIR is caused by the fluorination of the oxide shell surrounding the Al core [15]. This process was manipulated and proven to be accelerated with an Al-perfluoro tetradecanoic (PFTD) structure [7]. It was done by lowering the bond dissociation energy from its more sterically hindered structure. McCollum et al. examined the performance of the thermite-perfluoropolyether (PFPE) blends and concluded that they are highly dependent on the oxidizing agent [16]. These works show that fluoropolymers can promote reactivity via catalytic behavior of the Al_2O_3 shell, which improves the low-temperature surface reactions and aluminum sensitivity.

There have been several studies that extended methods for enhancing the reactive performance of Al systems with the addition of PVDF [17,18,43]. McCollum et al. varied the weight percentages of Al added to a PVDF film to study the specific combustion reaction [17]. Here, it was shown that the composite cannot sustain a self-propagating reaction at Al concentration up to 4 wt.% due to having a low fuel to oxidizer ratio. When Al concentration is increased toward stoichiometric mixtures, the energy release is increased, and the heat can travel more efficiently through the composite material resulting in a sustained self-propagating deflagration. Experiments like this show that the formulation of Al-fluoropolymer systems can be manipulated through composition and experimental parameters. Moreover, Row et al. manipulated nAl-fluoropolymer composite systems by sensitizing them using an external DC voltage [43]. This phenomenon was quantified using a drop-weight apparatus. The materials that were not subjected to an electric field did not ignite even at the highest impact energy tested. However, the applied DC voltage led to an increase in sensitivity in the energetic composites for all fluoropolymers used including a terpolymer of tetrafluoroethylene, hexafluoropropylene and vinylidene fluoride (THV), vinylidene fluoride and hexafluoropropylene (VDF-HFP) copolymer, and PVDF. It was also observed that this effect of sensitization diminished after the voltage was turned off for more than five seconds. This behavior could be explained by a property other than piezoelectricity. It could be described as a 'charge' effect since it dissipates with time similar a charged capacitor. Alternatively, the application of a DC voltage may result in the polarization within the electroactive phases of the piezoelectric material. Poling a β-phase PVDF film could lead to an increase in sensitivity and performance without the need for an external power source.

In this study, we combine the experiment and computational simulation to study the electrical charge generation and the ignition sensitivity of P(VDF-TrFE)/nAl composite films under applied impact force. We fabricated a nanocomposite energetic thin film and subjected them to drop-weight sensitivity tests in poled and unpoled states. The objectives are to (i) create a composite energetic material using P(VDF-TrFE) and nAl that can be poled and exhibit piezoelectric behavior, (ii) experimentally investigate the drop-weight impact sensitivity of the poled and unpoled films in order to quantify the electromechanical effect on the ignition sensitivity, and (iii) develop a computational model that allows us to model the flexoelectric and piezoelectric polarizations induced by the impact load and predict the film's ignition threshold based on multiple samples of a SEMSS (statistically equivalent microstructure sample set).

2. Materials and methods

2.1. Fabrication of the composite film

Nanoaluminum particles used in our samples were nominally 80 nm in diameter and purchased from Novacentrix. The active nAl content of the powders was 70%, as determined by differential scanning calorimetry and thermogravimetric analyzer (DSC/TGA) [44]. The 70/30 Poly(VDF-co-TrFE) (Vinylidene Fluoride and Trifluoroethylene Copolymer) powder was purchased from Arkema. The final film was composed of 10 wt.% in active nAl (or ~9% in nAl volume fraction) to ensure that the fabricated film was reactive. The P(VDF-TrFE) was poured into a solution of dimethylformamide (DMF) at a ratio of 1 gram of nAl to 5 mL of DMF. This mixture was then mixed using a high-energy ultrasonic mixer (Branson) at 15% ultrasonic amplitude for 1.5 min on, 1.5 min off for a total of 3 min on. After becoming a homogenous and transparent solution, the nAl was added and the mixture was sonicated for 1.5 min on, 1.5 min off, for a total mixing time of 9 min. Once the samples were well mixed, they were cast onto glass slides using a tape caster (MSK-AFA-HC100, MIT) with a heated bed set at 125 °C and a blade height of 1 mm. Tape casting method over other methods was preferred to ensure that the films have uniform thicknesses and are near full density, which are essential for the poling process discussed later. Other casting methods tried did not achieve similar results. The average thickness of the casted film was 85 µm after drying at a heated substrate for 15 min. The density of the

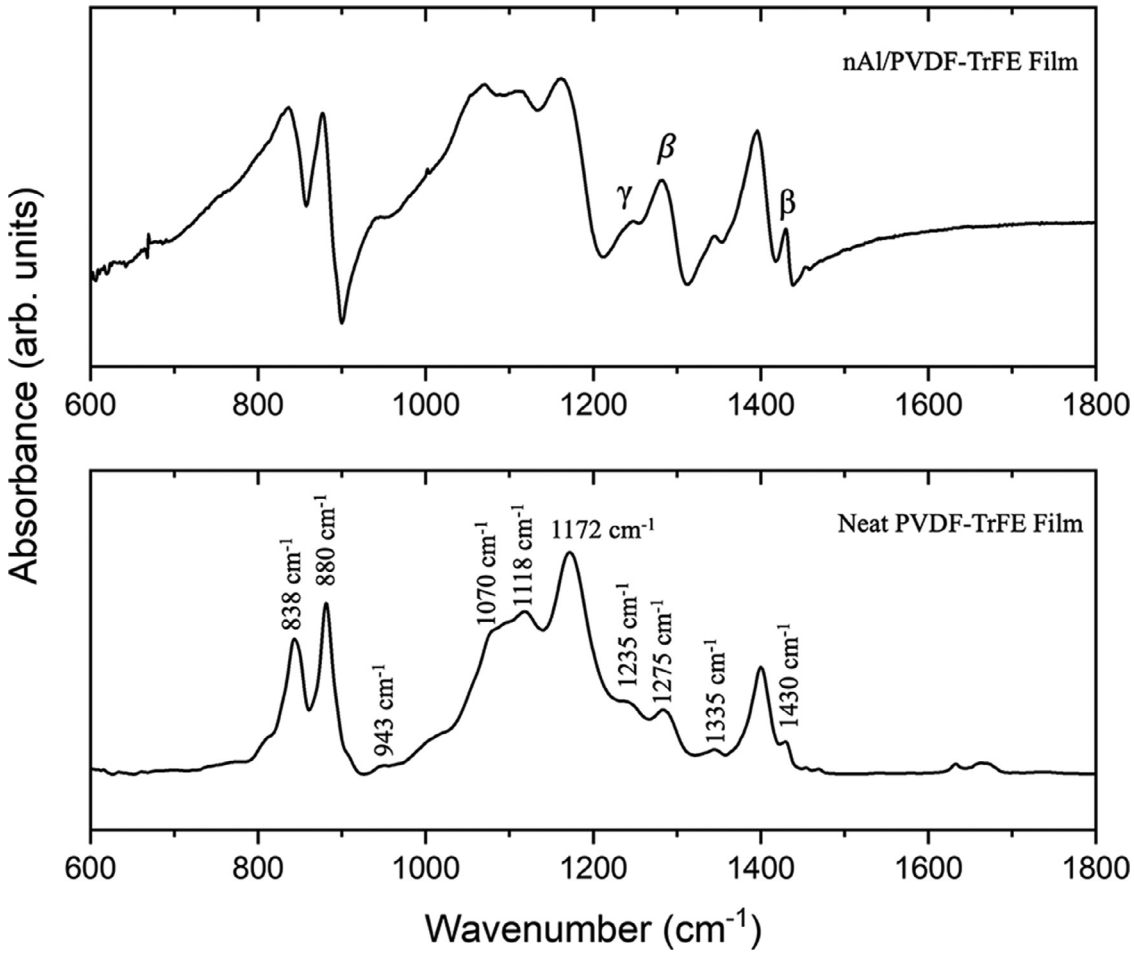

Fig. 1. FTIR spectra of P(VDF-TrFE)/nAl films and neat P(VDF-TrFE).

film was measured using Archimedes' principle (AGZN220, Torbal). Field-emission scanning electron microscopy (SEM) imaging was performed to observe the microstructure of the film's cross-section using a FEI Nova NanoSEM operating at 5 kV. The samples were coated with 20 nm thick platinum/palladium alloy before SEM imaging using a sputter coater (Cressington). Fourier Transform Infrared (FTIR) spectroscopy was used to assess the changes in the structure in films before and after the addition of nAl particles at a 2 cm^{-1} spectral resolution by averaging 32 scans using a Perkin Elmer Spectrum Two spectrometer (Diamond-ATR technique).

2.2. Electrical poling of the films

After the films were fabricated, a voltage potential was applied to the films in a process called electrical field poling. Indium tin oxide (ITO) glass slides (MSE Supplies) with conductive surfaces were used as electrodes to sandwich the film and establish the electric field. A glass slide with a 1 mm thickness was placed between the two ITO glasses to act as a dielectric barrier to prevent electrical breakdown. The ITO glass slides were connected to a power supply (ET40, Glassman), and up to 9 kV voltage was applied across the films prior to breakdown. An extensive poling process was conducted to attain the maximum piezoelectric constant (d_{33}) in the films. It was determined that the application of 8 kV for 5 min yields reproducible results while excessive poling duration does not increase the piezoelectric coefficient which was measured by Berlincourt type piezoelectric tester (PolyK Technologies). The effective applied electric field of 7.3 MV/m was calculated by dividing the applied voltage by the total thickness of the dielectric barrier and the sample.

The poled P(VDF-TrFE)/nAl films had an average d_{33} value of −5.45 pC/N with a standard deviation of 0.38 pC/N based on the Berlincourt type piezoelectric tester. Neat P(VDF-TrFE) films were able to attain a d_{33} coefficient of −30 pC/N with the same poling method. The addition of nAl created a new composite that was conductive and sensitive to electrical breakdown at magnitudes of electric fields. For this reason, it was expected that the P(VDF-TrFE)/nAl films would be less piezoelectric than commercially available PVDF polymers. The unpoled samples were confirmed to display no piezoelectric response.

2.3. Film characterization

Fourier-transform infrared spectroscopy (FTIR) scans were performed to identify the electroactive phases and their possible changes in the P(VDF-TrFE) before and after nAl addition. The absorbance spectra of the tape cast neat P(VDF-TrFE) and P(VDF-TrFE)/nAl films are shown in Fig. 1. The absorbance bands at around 875, 1070, 1170, and 1400 cm^{-1} are the common bands observed in PVDF regardless of the crystallographic phase [23,45]. The absorbance band explicitly assigned to electroactive β-phase is around 1275 cm^{-1} [23,45]. The band at around 1234 cm^{-1} is assigned to the electroactive γ-phase [23,45]. The peaks at around 840 and 1430 cm^{-1} can be assigned to both β- and γ-phases. The α-phase are characterized by the bands at around 763, 795, 976, 1210, and 1385 cm^{-1} [23,45]. The vibration bands in the absorbance spectra indicate that the electroactive γ- and β-phases

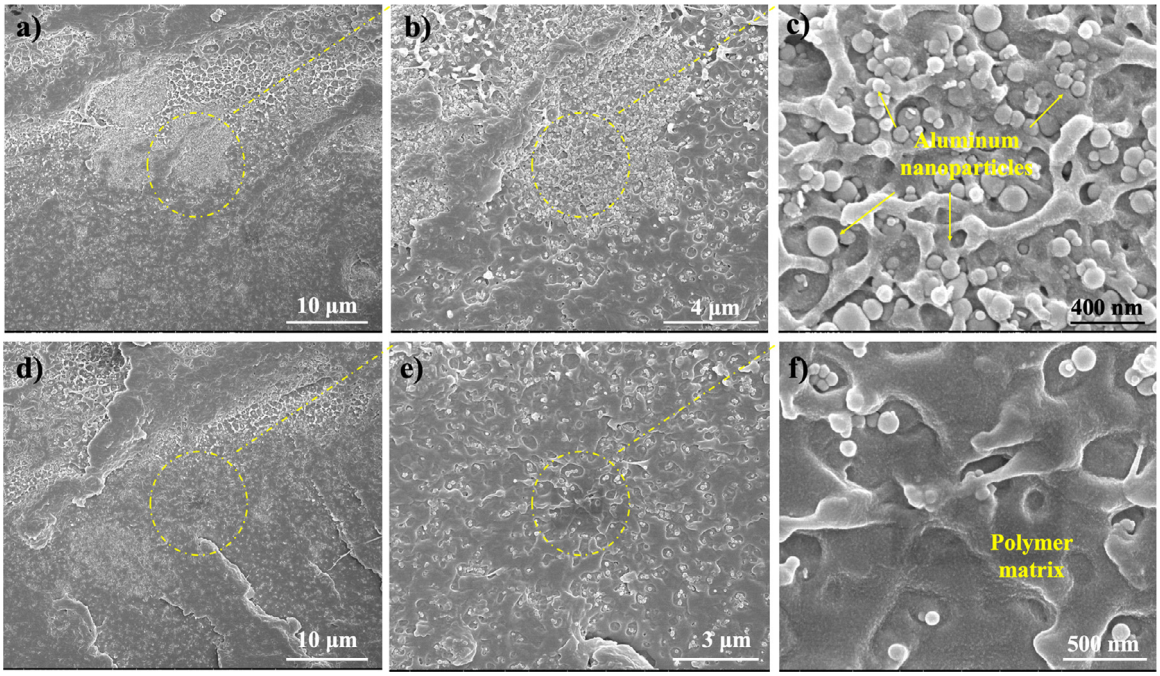

Fig. 2. Scanning electron micrographs of the P(VDF-TrFE)/nAl composite films showing: (a,d) the cross-section images of the sample with minimal porosity; (b,e) the smooth and rough surfaces with nAl particles dispersed throughout the polymeric matrix in microscale resolution; and (c,f) the clustered nAl particles within the polymeric matrix with fibrous polymer network surrounding the particles in nanoscale resolution.

are readily present and dominant in the tape cast neat P(VDF-TrFE) film as shown in Fig. 1. However, the absorbance bands pertaining to non-centrosymmetric α-phase are not prominent.

After the addition of nAl, it was observed that the relative intensity of peak at around 1275 cm^{-1} pertaining to the β-phase increases and the peak becomes more distinct. In addition, the peak pertaining to solely γ-phase has lower intensity than β-phase peak in contrary to neat film, which may suggest higher β-phase fraction among the electroactive phases. We note that the β-phase content within the entire polymer matrix can be quantified using a method as described in [26,46,47]. In this method, the absorbance value of α-phase at around 764 cm^{-1} and the absorbance value of β-phase at 840 cm^{-1} is used to quantify the content of phases. However, in our FTIR spectrum, the peaks pertaining to α-phase is not clearly distinguishable in the neat film possibly due to its low content in the neat film. Also, for the nAl added film, the absorbance spanning from 600 to 840 cm^{-1} is very broad, which prevents the detection of peak at 765 cm^{-1} for α-phase. Due to these reasons, we were not able to quantify the actual phase content of β-phase within the polymer matrix. Nevertheless, the FTIR results suggest that P(VDF-TrFE)/nAl films possess both electroactive γ- and β-phases, indicating that the films can be exhibit piezoelectricity via poling.

SEM micrographs were obtained from the cross-sections of the films to examine the microstructure. Representative images of the P(VDF-TrFE)/nAl-10 wt.% film dried at 125 °C are shown in Fig. 2. Lower resolution images in Fig. 2(a,d) show the cross-sections of the film with little to no porosity on a macroscopic scale. Higher-resolution microscale images shown in Fig. 2(b,e) depict both the smooth and relatively rough surfaces. In these microscale images, the nAl particles are visually confirmed to be dispersed throughout the P(VDF-TrFE) binder while maintaining low porosity. In addition, branches of the P(VDF-TrFE) binder surrounding the nanoparticles can be observed throughout the sample. The broken fibrous structure of the polymer is due to the sample preparation for imaging, where the samples were frozen and then shattered in liquid nitrogen.

The porosity of the films is controlled by the temperature of the tapecaster bed during casting. By raising the temperature of the drying bed, the DMF is evaporated out of the films at a more rapid pace and allows for the liquid mixture of P(VDF-TrFE)/nAl to form films with higher density. A nanoscale image in Fig. 2(c), which is taken from the rough area as marked in the image (b), shows a close-up view of the nAl particles distributed in the polymeric matrix. Some clusters of nanoparticles can be also observed. It is also noted that the nAl particles vary in size under ~100 nm. Another nanoscale image shown in Fig. 2(f) taken from the region marked in Fig. 2(e) confirms that the particles are well-dispersed within the relatively smooth P(VDF-TrFE) matrix. A drying temperature of 125 °C was found to consistently result in minimal porosity and was used to prepare the full density sample for solids loading experiments. This was also confirmed with an Archimedes density tester using the buoyancy technique. The results showed that the composite film was 97% of theoretical maximum density (TMD).

2.4. Drop-Weight experiment & high-speed imaging

The current widely used statistical test for determining the sensitivity of energetics is the Neyer D-optimal test [48]. This method is designed to determine the optimal testing level for sequential sampling based on the 'go' or 'no-go' response of the previous samples. Utilizing the commercial program SenTest^{TM} allows for a rapid determination of the height at which half of the samples were expected to ignite (here, this is referred to as the 50% drop-height). The distributions and confidence intervals resulting from these tests can then be used to compare the sensitivities of a wide range of energetic materials and compositions. However, due to differences in the design of impact machines, these measures should be generated for each material of interest on the same machine.

The drop-weight impact apparatus used is the BAM configuration (Bundesanstalt für Materialforschung) fall hammer by OZM Research to quantify impact sensitivity. This apparatus enables the application of a precisely controlled impact based on a specified

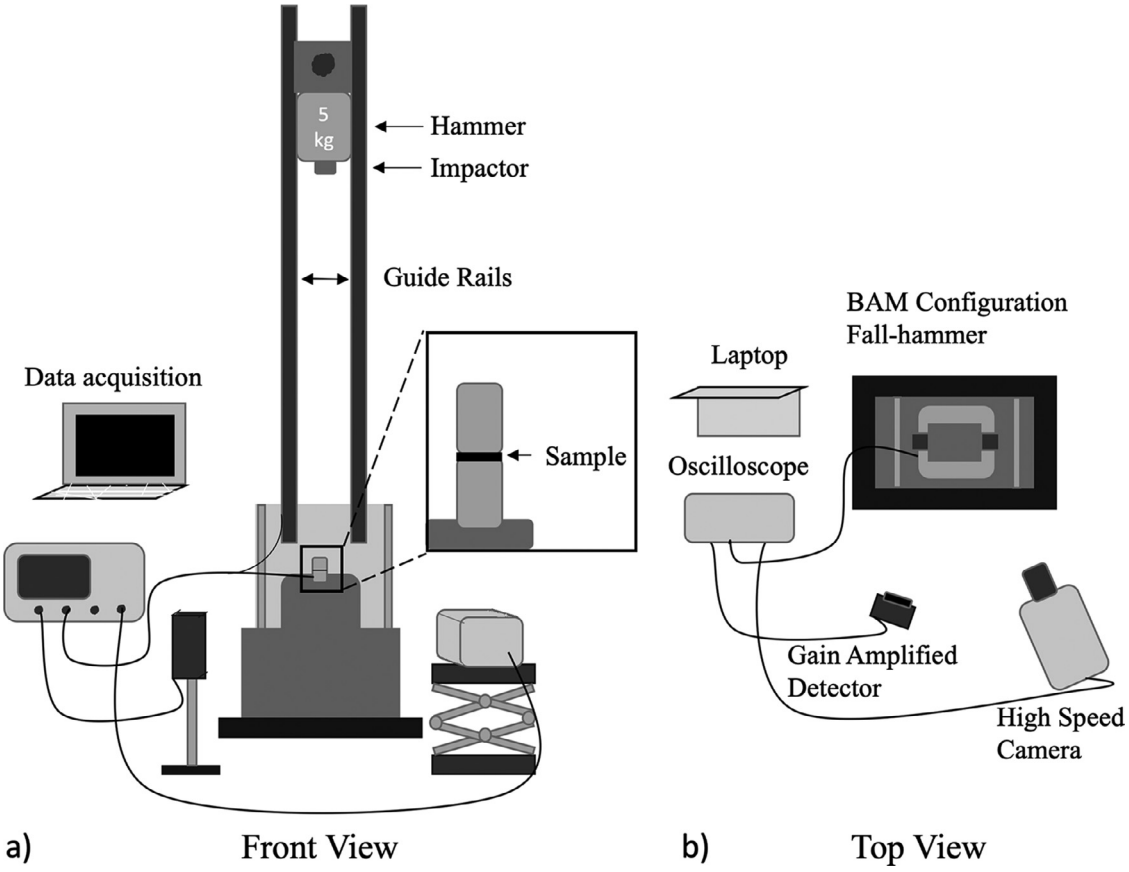

Fig. 3. A schematic illustration of the (a) front and (b) top views of the drop-weight experimental setup.

drop-height and hammer mass. The tower has a maximum drop-height of 1 meter and provides frictionless guide rails for the 5 kg hammer. The specified BAM configuration was engineered to minimize variability with the impactor orientation. This entails a sample holder consisting of a steel guide ring encapsulating two steel cylinders where the sample is placed in between. The results of the impact were categorized as either 'go' or 'no-go'. A 'go' represents a sample that ignited, while a 'no-go' represents a sample that did not ignite. Multiple drop-heights were tested to determine the minimum ignition energy (MIE), or equivalently here the minimum drop-height. The distances were determined using the Neyer SenTest^{TM} software for each sample test. The recommended drop-height is populated based on the result of the previous test. The software does not indicate whether a sufficient number of samples have been tested. Therefore, the approach taken to end the test was to stop after the standard deviation monotonically decreased over the course of five tests. When the test was completed, the material's 50% probability of explosion drop-height and standard deviation values were extracted for further analysis.

The ignition time (or time-to-ignition), t_{IGN}, was also computed using the same drop-weight apparatus. However, the procedure consisted of testing samples at five drop-heights starting at 20 cm and increased to 100 cm at equal increments. The impact time was determined based on the film's pressure output signals. A voltage probe was connected to the top and bottom metal contacts of where the sample was placed to detect the voltage produced with an oscilloscope. One lead was attached to the bottom pin and the other was placed on the rail in direct connection with the metal hammer. On the other hand, the ignition event was determined using Ge Switchable Gain Amplified Detector from Thorlabs, a photodiode in infrared (IR) wavelength, paired up with a high-speed camera. A Phantom v2012 high-speed camera (Vision Research) was used in conjunction with the experiment to interpret the signals from the oscilloscope at a rate of 100,000 fps (or frames per second). The time delay between the initial sign of impact (from the pressure signal) and the initiation of the ignition event (from the IR signal) represents the ignition time. Fig. 3 shows the schematic of the experimental setup for drop-weight and ignition time measurements.

2.5. Microstructure generation & simulation setup

To analyze the ignition sensitivity of a poled and an unpoled P(VDF-TrFE)/nAl film subjected to mechanical impact, a microstructure model with randomly distributed Al particles has been generated. Similar to the samples tested in the experiment, the microstructure model has a film thickness of 85 μm and comprises aluminum particles that are embedded within the P(VDF-TrFE) binder. The material properties, including the mechanical and dielectric properties of the constituents, are delineated in Table 1, and the piezoelectric and the transverse flexoelectric constants of the P(VDF-TrFE) binder are listed in Table 2.

Similar to the experiment, the particle volume fraction (i.e., the volumetric ratio of the cumulative particles to the total composite film) is $\eta = 9\%$. Although the particle size in the actual samples varies (diameters between 64 and 78 nm) and shows a normal distribution based on small-angle X-ray scattering analysis [51], the present model treatment offers simplicity [52]. In order to enhance computational efficiency while preserving the full specimen thickness, the Al particles have been modeled as solid circles with a diameter of 2.26 μm (~30 times the average size in the actual material). This simplification has been independently verified to yield similar electrical response within the microstructure and ignition threshold as a model with the actual particle size, as the threshold

Table 1
Physical, dielectric, and elastic properties of the film constituents [49,50].

Material	ρ [kg/m^3]	κ_{ij} /ϵ_0	E_{bd} [MV/m]	E [GPa]	ν	σ_y [MPa]
P(VDF-TrFE)	1880	10	400	2.01	0.27	...
Aluminum	2702	...	...	70	0.33	140
Al_2O_3 shell	3960	9.9	≥500	370	0.22	...

Table 2
Piezoelectric and flexoelectric coefficients of the P(VDF-TrFE) binder [39,49].

Material	d_{31} [pC/N]	d_{32} [pC/N]	d_{33} [pC/N]	d_{15} [pC/N]	d_{24} [pC/N]	μ [nC/m]
P(VDF-TrFE)	1.89	1.89	−5.45	−4.19	−4.19	191

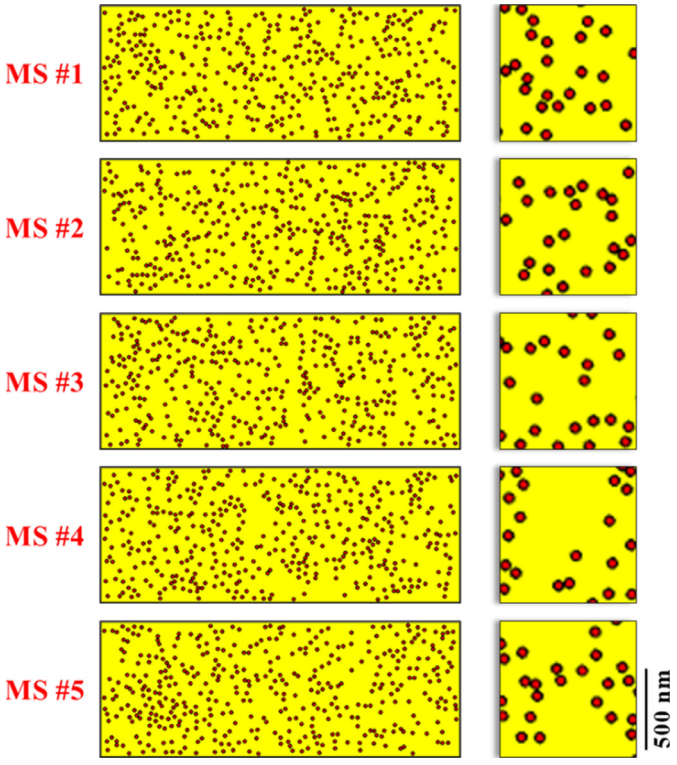

Fig. 4. Five random microstructure instantiations in a statistically equivalent microstructure sample set (SEMSS). The enlarged inset images on the right show the explicit consideration of the Al core and the Al_2O_3 shell.

depends on the ratio of critical particles (the threshold criteria is further delineated later in the manuscript).

The ratio of the particle's core radius (Al) to the shell thickness (Al_2O_3) is 11.12, consistent with that in the experimental samples, whose average core radius and shell thickness are 36.7 nm and 3.3 nm, respectively. Additionally, to account for the statistical variations in the material ignition sensitivity due to intrinsic microstructure randomness, a statistically equivalent microstructure sample set (SEMSS) consisting of five random but similar microstructures has been generated, as shown in Fig. 4.

The compressive impact load from the hammer's drop-weight (5 kg in mass) is effected by prescribing a monotonic velocity ($v_y = -\sqrt{2gh_0}$) across the top surface of the microstructure, as illustrated in Fig. 5 (here, $g = 9.81$ m/s^2 is the gravitational acceleration constant). The bottom surface of the microstructure is mechanically constrained and electrically grounded ($\varphi = 0$). Specifically, there is no normal displacement ($u_y = 0$) perpendicular to the bottom surface and the tangential displacement (u_x) parallel to the bottom surface is permitted and obtained as part of the computational solution. The right end surface is charge-free and traction-free and the left end surface is a vertically symmetric boundary with $u_x = 0$ and u_y obtained as part of the solution. This symmetric boundary condition at the left end surface allows only half of the overall specimen to be explicitly resolved. All constituents in the microstructure are initially stress-free and at rest. The microstructure is a two-dimensional model, and the generalized plane-strain condition is assumed. Finally, the simulation analysis is implemented using COMSOL Multiphysics (v5.4).

2.6. Governing equations & constitutive relations

The electrostatic response of the material is governed by the conservation of charge (Gauss's Law). The quasi-static mechanical response is governed by the conservation of momentum. The equations are

$$\begin{cases} \mathrm{div}(\boldsymbol{D}) = \nabla \cdot \boldsymbol{D} = q_v^\circ, \\ \mathrm{div}(\boldsymbol{\sigma}) = \nabla \cdot \boldsymbol{\sigma} = -\boldsymbol{b}_v, \end{cases} \tag{1}$$

where $\boldsymbol{D}$ and q_v° denote, respectively, the electric displacement vector and free-charge density per unit volume, $\boldsymbol{\sigma}$ and $\boldsymbol{b}_v$ denote the mechanical stress tensor and body-force vector per unit volume, respectively. In the present analysis, $q_v^\circ = 0$ and $\boldsymbol{b}_v = \boldsymbol{0}$.

The electric displacement consists of a dielectric polarization term caused by the induced dipole moment, a piezoelectric polarization term caused by the local stress, and a flexoelectric polarization term caused by the local strain gradients. The constitutive relation is

$$D_i = \kappa_{ik} E_k + d_{ikl}\sigma_{kl} + \mu_{ijkl}\frac{\partial \varepsilon_{jk}}{\partial x_l}, \tag{2}$$

where E_k and $\partial \varepsilon_{jk}/\partial x_l$ denote the electric field and strain gradient, respectively; κ_{ik}, d_{ikl}, and μ_{ijkl} represent the absolute permittivity, piezoelectric coefficient, and flexoelectric coefficient tensors, respectively. An isotropic permittivity is assumed for all constituents in the microstructure. The electric field vector can be further expressed as $E_k = -\partial\varphi/\partial x_k$ with φ denoting the scalar electric potential field in the material.

The Green-Lagrange finite strain tensor $\boldsymbol{\varepsilon}$ can be related to the displacement $\boldsymbol{u}$ via

$$\boldsymbol{\varepsilon} = \frac{1}{2}\left(\boldsymbol{F}^{\mathrm{T}}\boldsymbol{F} - \hat{\boldsymbol{I}}\right) = \frac{1}{2}\left[(\nabla \boldsymbol{u}) + (\nabla \boldsymbol{u})^{\mathrm{T}} + (\nabla \boldsymbol{u})^{\mathrm{T}}(\nabla \boldsymbol{u})\right], \tag{3}$$

where $\boldsymbol{F}$ and $\hat{\boldsymbol{I}}$ represent the deformation gradient and the identity tensors, respectively; and $\boldsymbol{u} = \boldsymbol{u}(\boldsymbol{x})$ indicates the displacement vector at a material point, $\boldsymbol{x}$.

As the deformation is assumed to be quasi-static, the rate-dependence of the constitutive behaviors is not considered. The coupled electromechanical stress tensor can be written as

$$\sigma_{ij} = C_{ijkl}\varepsilon_{kl} - d_{kmn}C_{mnij}E_k + \mu_{lijk}\frac{\partial E_l}{\partial x_k}, \tag{4}$$

where C_{ijkl} represents the elastic stiffness tensor.

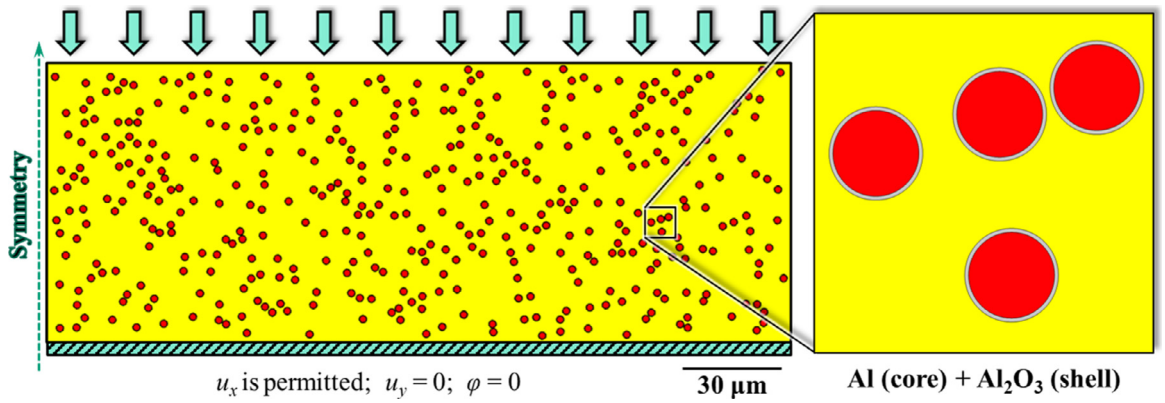

Fig. 5. An illustration of the mechanical and electrical boundary conditions applied to the P(VDF-TrFE)/nAl composite model. The microstructure has a particle volume fraction of $\eta = 9\%$.

3. Results and discussion

3.1. Impact sensitivity

The experimentally measured results for the films are plotted in Fig. 6 as cumulative density functions (CDF) based on the estimated drop-height, standard deviation, and an assumed normal distribution. To satisfy the parameters in the Neyer SenTest^{TM}, a total of 45 and 51 samples were tested for unpoled and poled films, respectively. It is shown that the poled films are more sensitive to impact than the unpoled films with no piezoelectric response. The drop-height for a 50% probability of ignition for the poled samples was 10.41 cm, whereas the drop-height for the unpoled samples was 11.30 cm. The 0.89 cm difference in drop-height correlates to an increased sensitivity of the poled films by ~8%. Precautions were taken to minimize the experimental errors such as using new BAM sample holders for consistent holder/sample interface per each test and using a large number of samples to establish statistical significance. In addition, the sample variation was minimized by taking films from the same batch such that poled and unpoled samples would have similar composition and porosity. Therefore, the small difference in sensitivity can be attributed to the piezoelectric effect.

The initiation of impact is defined as the moment when the hammer contacts the top steel cylinder and begins to compress the sample. This event coincides with the event of impact signaled by the voltage produced by the sample itself. It is important to emphasize that we are using the reactive film simultaneously as a time-of-arrival gage. Fig. 7 illustrates the time-lapse of the subsequent ignition event for an unpoled film with a drop-height of 40 cm. The flash, if present, is indicated for each timeframe by a yellow arrow. For this particular test, the ignition occurs at about 130 μs after the impact as determined by an infrared sensor and can be observed as a faint flash in the high-speed video images at 150 μs as shown in Fig. 7. A similar event takes place for the poled P(VDF-TrFE)/nAl film, but the ignition occurs ~10 μs earlier. This difference is investigated further in a later section.

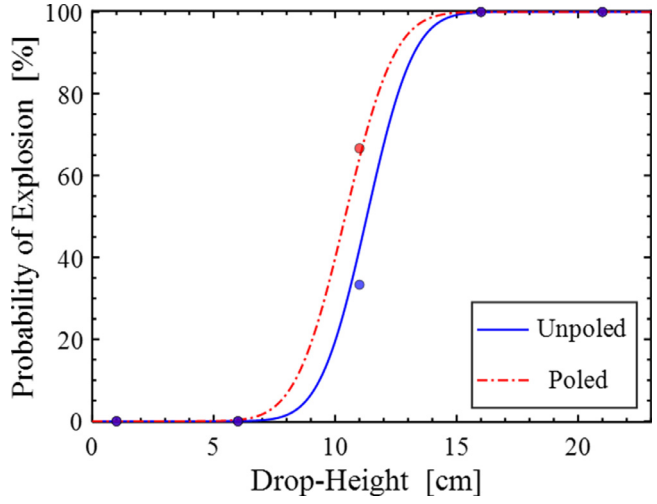

Fig. 6. Cumulative distribution functions of explosion probability as a function of drop-height for poled and unpoled samples.

Fig. 8 displays an example of the output voltage from the piezoelectric sample along with the signal from the photodiode detecting at the infrared wavelength. The time on the *x*-axis in Fig. 8 is taken from the oscilloscope which is triggered with the piezoelectric curve and keeps the recordings before the event to ensure nothing is overlooked. The ignition delay is calculated by subtracting the impact start time from the ignition start time which is represented by the first sign of movement from the curves. On the pressure curve, there is a lot of electrical activity observed after the first sign of impact. This signal cannot be attributed to one factor but is a result of the sample holder movement and electromechanical response as the sample is being compressed. Also, the magnitude of the output voltage was quantified by the oscilloscope, but these measurements were not used in this experiment. There is no measured voltage when no sample is present. The same applies for the infrared signal. The first sign of thermal release is chosen to describe the ignition initiation even though there are some cases where ignition is captured more than once. The electromechanical properties of the P(VDF-TrFE) in the energetic composite allowed for a time-of-arrival measurement to be made with an instantaneous response for both the poled and unpoled films.

3.2. Prediction of dielectric breakdown

We focus on the electric process because analyses show that plastic yielding and inelastic dissipation-induced temperature rises are negligible under the conditions of our experiments. Therefore, the ignition is due to electric field induced dielectric breakdown and subsequent localized conductive heating. To analyze the ignition sensitivity of the P(VDF-TrFE)/nAl composite film under the impact loading, the induced electrical responses are first examined. Fig. 9 shows the electric potential and electric field distributions for both poled and unpoled films under the external impact load with a drop-height (h_0) of 20 cm. While the level of overall voltage generated (φ) is small within unpoled films, poled films show

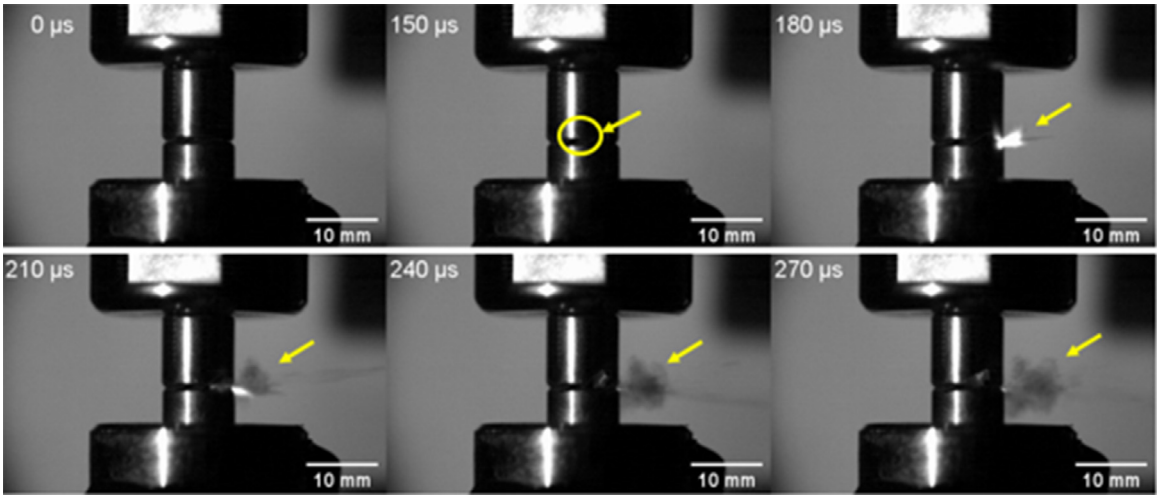

Fig. 7. High-speed camera images showing the progression of the ignition event for an unpoled P(VDF-TrFE)/nAl film under a drop-height of 40 cm.

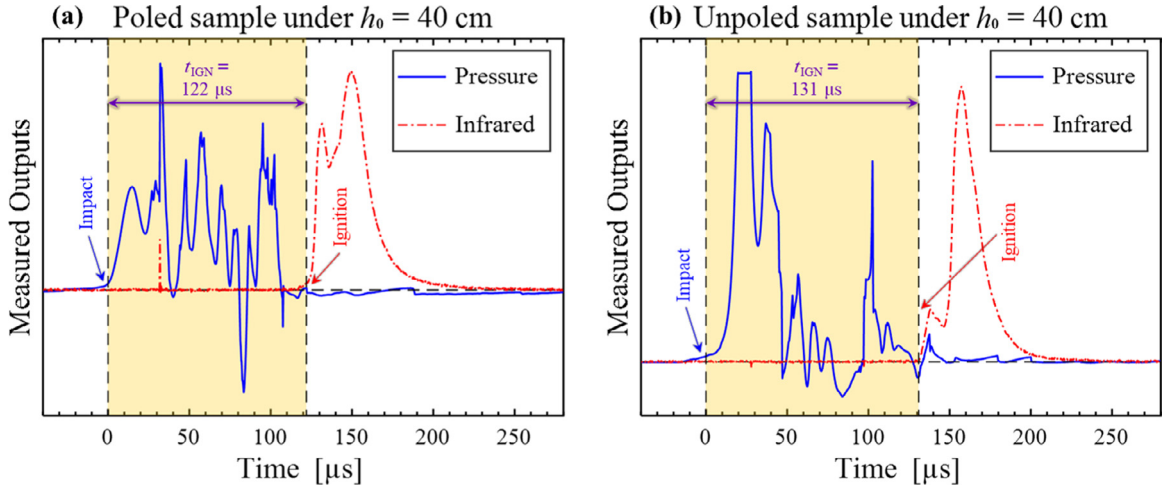

Fig. 8. Pressure and infrared detector signals as a function of time for (a) poled and (b) unpoled P(VDF-TrFE)/nAl films under a drop-height of 40 cm.

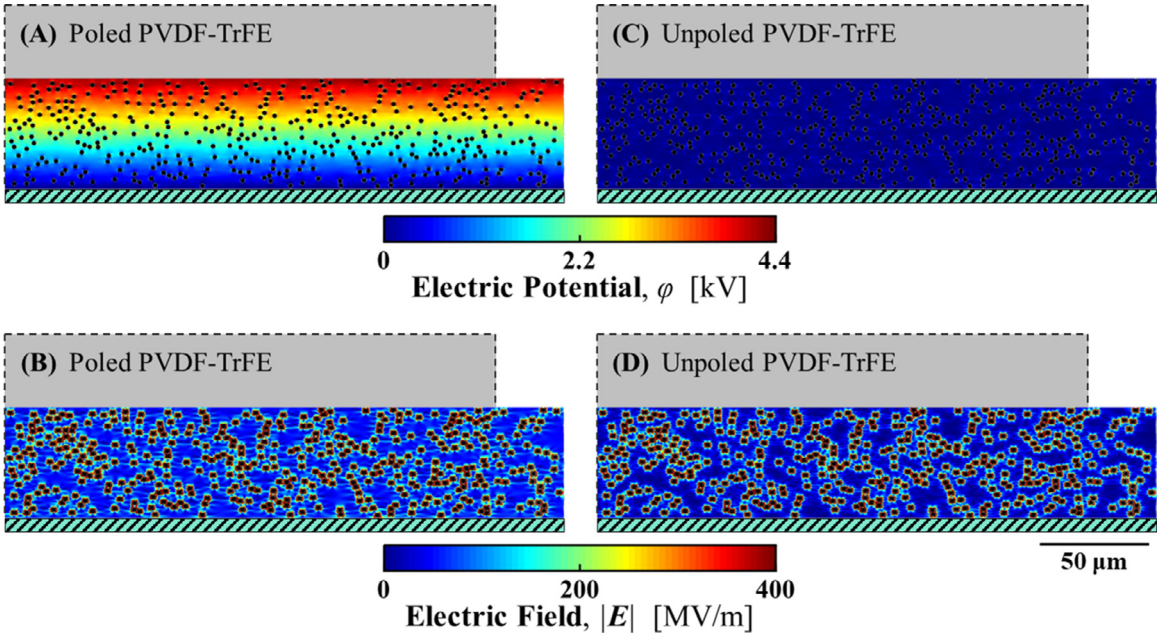

Fig. 9. Distributions of induced electric potential and electric field within (a,b) a poled and (c,d) an unpoled film for the microstructure shown in Fig. 5. The deformation corresponds to a drop-height of $h_0 = 20$ cm at $t = 111$ µs.

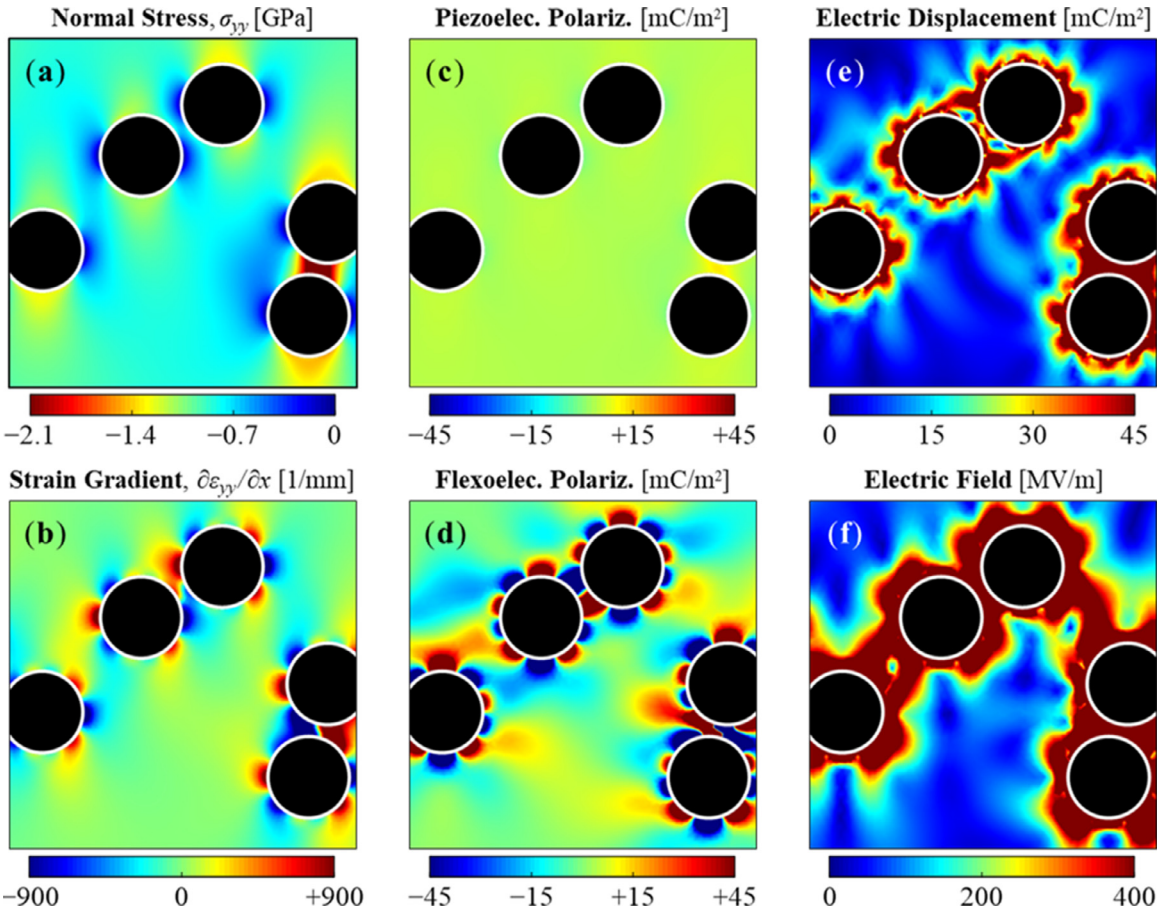

Fig. 10. Inset view of the electromechanical responses of poled film near the particles at t = 111 μs for h_0 = 20 cm. (a) Normal stress along y-direction, (b) transverse strain gradient, (c) piezoelectric polarization along y-direction, (d) flexoelectric polarization along y-direction, (e) electric displacement magnitude, and (f) electric field magnitude.

an appreciable voltage upon impact, owing to the binder's piezoelectric properties.

Several electromechanical quantities, including the underlying polarization and the resulting electric field, are also delineated in Fig. 10 for a poled film at t = 111 μs under a drop-height of 20 cm. The stress and strain gradient near the binder/particle interfaces induce piezoelectric and flexoelectric polarization, respectively. While the piezoelectric polarization depends on whether the film is poled or not, significant flexoelectric polarization is developed near the particle interfaces in both the poled and unpoled films, owing to their high strain gradients. For poled films as an example, the binder experiences a high interfacial enhancement (i.e., the ratio of the local interfacial response to the average bulk response in the binder) of electric displacement (∼8.2) and electric field (∼6.0).

Further, Fig. 11 illustrates the temporal evolution of the E-field for a poled film for a drop-height of 20 cm. It can be seen that the interfacial E-field near the particles rises over time and eventually reaches the breakdown strength of the P(VDF-TrFE) binder (E_{bd} = 400 MV/m). Here, it is also noted that the E-field evolution for an unpoled film is similar to that for a poled film, albeit with lower magnitude of E-field due to the absence of piezoelectric contribution. The comparison between the poled and unpoled films is illustrated in Fig. 9(b,d) and further delineated later in the manuscript.

The ignition sensitivity of the film is characterized by predicting the likelihood of dielectric breakdown along the binder/particles interfaces. It is noted that several nonlinear processes have not been explicitly considered as their influence is assumed to be inconsequential as follows. First, the heat dissipated by the electrical discharge and subsequent heating upon dielectric breakdown is not explicitly modeled here. Instead, we focus on the attainment of sufficient E-field strength for local dielectric breakdown and use this the condition as a measure for the ignition threshold. Once breakdown occurs, the localized Joule heating results in hotspots that set in motion the chemical reactions that eventually evolve into large scale ignition and the emission of light measured in the experiments. Since conductive heating occurs rapidly relative to the time scales of mechanical loading and evolution of chemistry upon hotspot generation and since breakdown is a threshold event leading to the observation of light emission associated with ignition in the experiment, the time to breakdown can be used as a measure for quantifying the ignition sensitivity. This is perhaps the earliest event in the chain of processes leading to ignition that can be used for this purpose. As such, we define this earliest time to be when the E-fields of sufficient Al particle interfaces reach the breakdown strength. This treatment obviates the need for explicit modeling of the complex post-breakdown process, which requires a multiphysics analysis of the mechanisms contributing to the thermal runaway and ultimately the ignition of the energetic films. Here, the primary focus of this threshold analysis is limited to the pre-ignition reaction (PIR) stage. The likelihood of interfacial breakdown is quantified as the extent to which the interfacial E-field reaches or exceeds the binder's breakdown strength.

It is also useful to point out that, the inelastic dissipation due to viscoelasticity of the P(VDF-TrFE) binder and viscoplasticity of the nAl particles was evaluated separately in a dynamic, thermomechanical (e.g., elastoviscoplastic-viscoelastic) analysis. Specifically, the viscoelasticity of the binder was modeled using the Standard Linear Solid model (SLS). The elastic-viscoplastic response of the

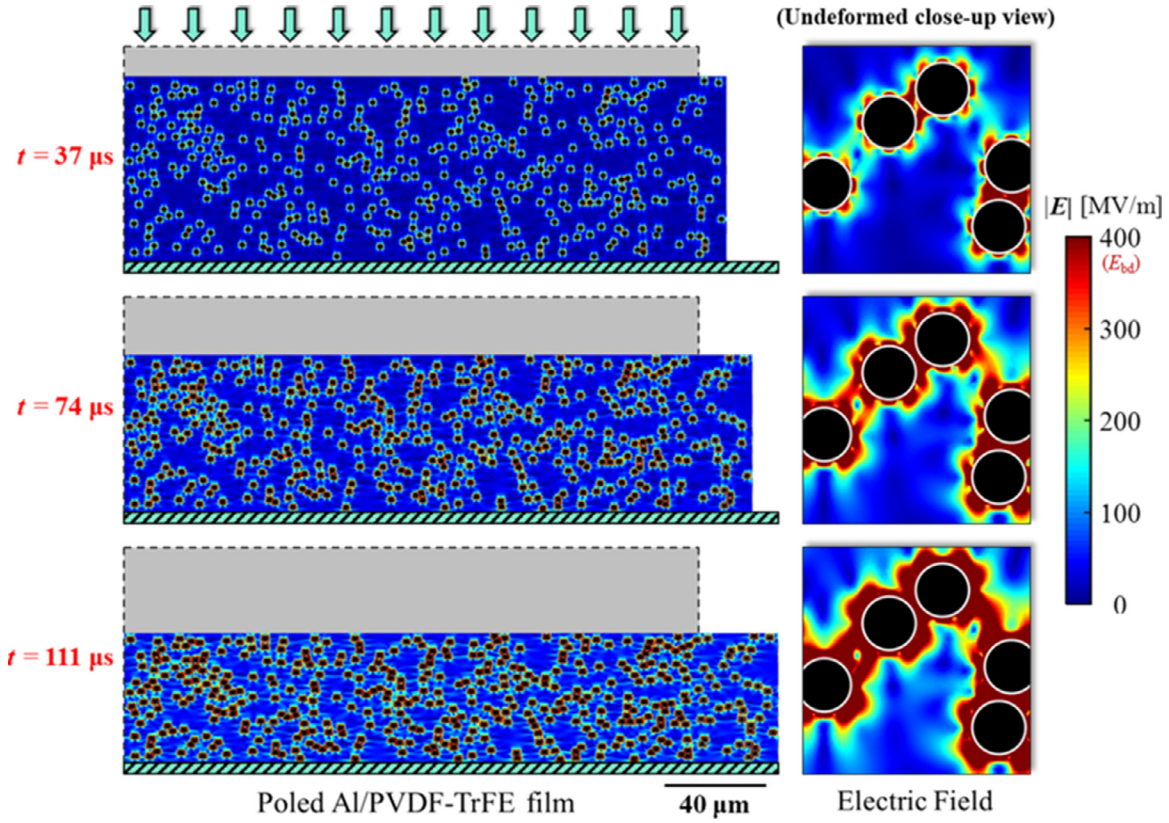

Fig. 11. Evolution of the electric field magnitude ($|E|$) within the poled binder under $h_0 = 20$ cm.

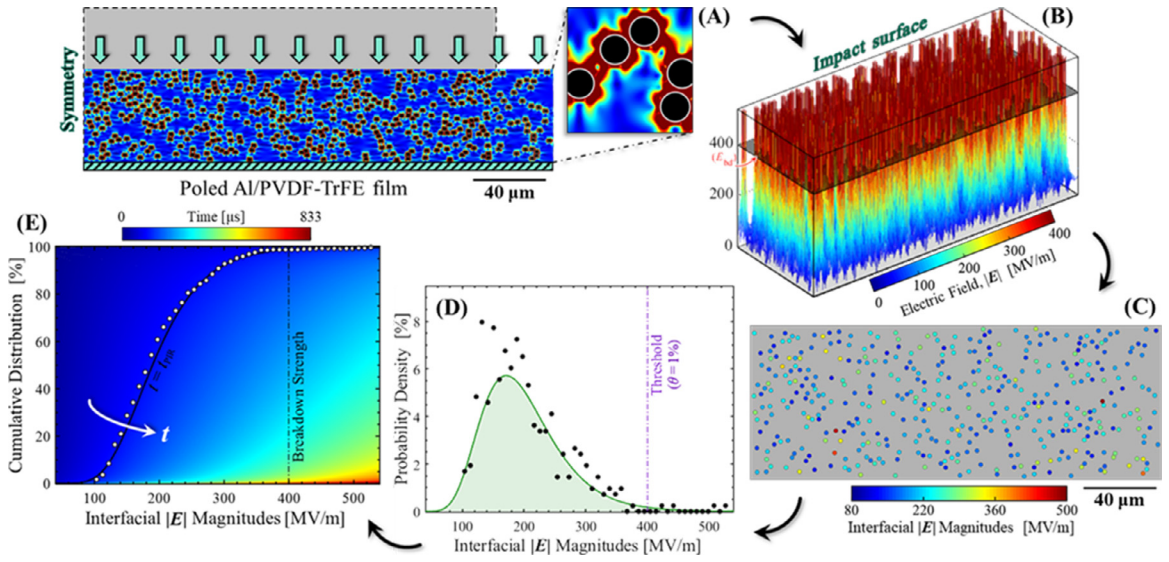

Fig. 12. (a) Distribution of induced E-field in a poled film under $h_0 = 20$ cm. (b) An illustration of the E-field with the regions whose local E-field exceeds the breakdown strength identified. (c) Particle distribution in the undeformed configuration with particle colors indicating the interfacial E-field magnitude. (d) The corresponding PDF with a lognormal distribution fit. (e) Time history map of the CDF for the interfacial E-field strength with the solid curve representing the CDF at $t = t_{\mathrm{PIR}}$.

particles was modeled using the Perzyna model and the Ludwik model for isotropic hardening. The highest temperature rise caused by the two mechanisms is on the order of only ~1 K in the Al particles under a drop-height of 100 cm. This shows that the heating due to mechanical dissipation is negligible for drop-heights between 20 and 100 cm, and it is not a factor in the present study of ignition sensitivity.

In Fig. 12, the procedures for systematically determining the ignition threshold in terms of the time to pre-ignition breakdown, or time-to-PIR (t_{PIR}), are outlined. Based on the impact-induced E-field, the regions whose local binder E-field exceeds the breakdown strength of the binder are first identified. Next, the interfacial E-fields are evaluated for each particle by computing the geometric mean of the local E-field distribution along with the individual particle interfaces. The probability density function (PDF) and the cumulative distribution function (CDF) are then plotted by assuming that the interfacial E-fields follow a lognormal distribution. Based on the time history map of the CDF, the t_{PIR} is predicted by solving

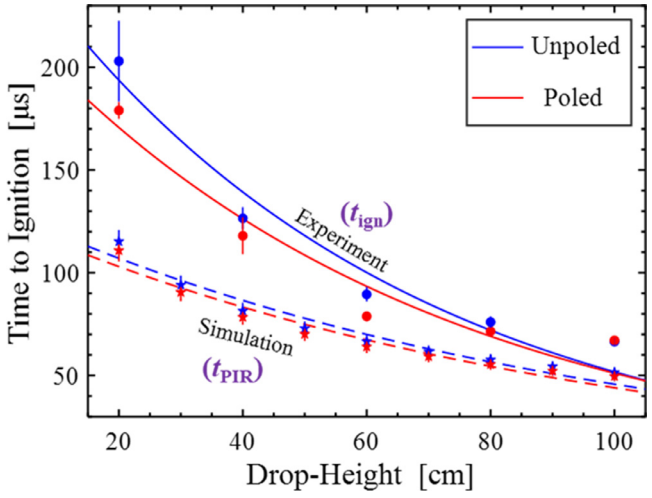

Fig. 13. Comparison of the predicted time-to-PIR t_{PIR} (dashed lines) and the experimentally measured time-to-ignition t_{IGN} (solid lines) for the sets (SEMSS) of poled and unpoled P(VDF-TrFE)/nAl films examined.

for the time at which the CDF equals 99% (or when the rightmost θ = 1% of the total area underneath the PDF is located at the breakdown strength). Here, θ denotes the specified threshold level and its baseline value has been set to θ = 1%. The equations for PDF and CDF are as follows, respectively.

$$p(|\boldsymbol{E}|) = \frac{1}{s_{LN}|\boldsymbol{E}|\sqrt{2\pi}} \exp\left\{\frac{-[\ln(|\boldsymbol{E}|) - m_{LN}]^2}{2s_{LN}^2}\right\}, \quad (5)$$

$$P(|\boldsymbol{E}|) = \frac{1}{2}\left\{1 + \mathrm{erf}\left[\frac{\ln(|\boldsymbol{E}|) - m_{LN}}{s_{LN}\sqrt{2}}\right]\right\}, \quad (6)$$

where $m_{LN} \equiv \ln(m^2/\sqrt{m^2+s^2})$ and $s_{LN} \equiv \sqrt{\ln[1+(s/m)^2]}$.

The threshold or t_{PIR} has been determined for drop-heights between 20 cm and 100 cm and compared to the experimentally measured time-to-ignition or observation of light emission. As indicated by the exponential regression curves of the time-to-PIR (t_{PIR}) and ignition time (t_{IGN}) shown in Fig. 13, the predicted thresholds for both poled and unpoled films decrease monotonically as drop-height is increased, showing similarities to the experimentally measured ignition times. Moreover, poled films have slightly quicker time-to-PIR than unpoled films, owing to the contribution of piezoelectric properties to the local *E*-field. In the case of P(VDF-TrFE)/nAl films, however, poling is shown to render a tenuous effect on the sensitivity, as the predicted threshold for poled films only differs from that of unpoled films by ~3.8%. The reason for this weak effect is that the electromechanical polarization predominantly stems from the relatively strong flexoelectric properties of the binder.

4. Summary and conclusion

Understanding the detailed electromechanical response (such as stress, flexoelectric and piezoelectric polarizations, and electric field) can be crucial for predicting the ignition sensitivity of a P(VDF-TrFE)/nAl film subjected to impact loading. In the present study, we have explored and delineated the set of experimental test methodologies as well as a systematic approach to quantifying the film's ignition sensitivity using computational simulation results and probabilistic analyses. To prepare the samples, we fabricated multiple composites of poled (attainable $|d_{33}|$ = 5.45 pC/N) and unpoled P(VDF-TrFE) films with a thickness of 85 μm and nAl volume fraction of 9%. The experimental outcome consists of a probabilistic determination of the minimum impact load required to cause ignition and a quantification of the ignition times for characterizing the ignition sensitivity. The poled samples were shown to be ~8% more sensitive than unpoled samples. Microstructure-explicit simulations were also performed and showed that the film's underlying flexoelectric and piezoelectric properties can influence the ignition sensitivity by enhancing the interfacial electric field beyond the breakdown strength, resulting in local temperature rise near the nAl particles and ultimately triggering ignition reactions.

The effect of poling the composite films was investigated by comparing the ignition delays of poled and unpoled films after impact. Experimental and computational results both indicate that poled films require a shorter time-to-ignition (e.g., by ~4% at h_0 = 20 cm), especially at low drop-heights. Nonetheless, a detailed computational analysis of the two underlying electromechanical properties revealed that flexoelectricity is the principal mechanism in P(VDF-TrFE)/nAl films in particular and that piezoelectricity can be used to further modulate (or "fine-tune") the ignition sensitivity. Owing to the flexoelectric properties present in both poled and unpoled P(VDF-TrFE)/nAl films, the interfacial enhancement of the *E*-field can be as high as ~6.0, which is sufficient to cause local breakdown near the nAl particles. Overall, the experiment and simulation showed good agreement in their trends and demonstrated that altering the electromechanical properties of the energetic films can be a viable option for tailoring the ignition sensitivity. If a broader range of d_{33} values can be examined for the energetic composites, then the sensitivity may potentially be more tunable with piezoelectricity. Moreover, the effect of flexoelectricity may be explicitly studied in future experiments by enhancing the flexoelectric coefficients to further influence the local *E*-field near the particles.

Finally, we note that in the present computational analysis, the subsequent events following the pre-ignition stage, including the heat dissipations from local breakdown and the exothermic ignition reactions, have not been modeled here. Computational results that explicitly model the breakdown process and the chemical reactions among the individual constituents may be reported in future papers.

Declaration of competing interest

The authors declare that they have no known competing financial interests or personal relationships that could have appeared to influence the work reported in this paper.

Acknowledgments

This research was sponsored by the Air Force Office of Scientific Research Award No: FA9550–19–1–0008 (Program Manager: Dr. Mitat Birkan). Any opinions, findings, conclusions, or recommendations expressed in the article are those of the authors and do not necessarily reflect the views of the United States Air Force.

References

[1] L.E. Fried, M.R. Manaa, P.F. Pagoria, R.L. Simpson, Design and synthesis of energetic materials, Annu. Rev. Mater. Res. 31 (2001) 291–321.
[2] P.F. Pagoria, G.S. Lee, A.R. Mitchell, R.D. Schmidt, A review of energetic materials synthesis, Thermochim. Acta. 384 (2002) 187–204.
[3] Y. Wei, R. Ranjan, U. Roy, J.H. Shin, S. Menon, M. Zhou, Integrated lagrangian and eulerian 3D microstructure-explicit simulations for predicting macroscopic probabilistic SDT thresholds of energetic materials, Comput. Mech. 64 (2019) 547–561.
[4] S. Zeman, M. Jungová, Sensitivity and Performance of Energetic Materials, Propell. Explos. Pyrot. 41 (2016) 426–451.
[5] D.N. Collard, T.J. Fleck, J.F. Rhoads, S.F. Son, Tailoring the reactivity of printable Al/PVDF filament, Combust. Flame 223 (2021) 110–117.

[6] L. Bao, W. Zhang, X. Zhang, Y. Chen, S. Chen, L. Wu, R. Shen, Y. Ye, Impact of MWCNT/Al on the combustion behavior of hydroxyl ammonium nitrate (HAN)-based electrically controlled solid propellant, Combust. Flame 218 (2020) 218–228.
[7] K.S. Kappagantula, C. Farley, M.L. Pantoya, J. Horn, Tuning energetic material reactivity using surface functionalization of aluminum fuels, J. Phys. Chem. C 116 (2012) 24469–24475.
[8] F.B. Koehler, M.T. Langhenry, Summers. Matt H, J.K. Villarreal, T.W. Villarreal, Electric propellant solid rocket motor thruster results enabling small satellites, 30th AIAA/USU Conference on Small Satellites, 2017 paper SSC17-II-02.
[9] R.M. Martin, Piezoelectricity, Phys. Rev. B 5 (1972) 1607.
[10] N.A. Shepelin, A.M. Glushenkov, V.C. Lussini, P.J. Fox, G.W. Dicinoski, J.G. Shapter, A.V. Ellis, New developments in composites, copolymer technologies and processing techniques for flexible fluoropolymer piezoelectric generators for efficient energy harvesting, Energy Environ. Sci. 12 (2019) 1143–1176.
[11] G.S. Neugschwandtner, R. Schwödiauer, S. Bauer-Gogonea, S. Bauer, Large piezoelectric effects in charged, heterogeneous fluoropolymer electrets, Appl. Phys. A-Mater. 70 (2000) 1–4.
[12] T.R. Sippel, S.F. Son, L.J. Groven, Aluminum agglomeration reduction in a composite propellant using tailored Al/PTFE particles, Combust. Flame 161 (2014) 311–321.
[13] T.R. Sippel, S.F. Son, L.J. Groven, Altering reactivity of aluminum with selective inclusion of polytetrafluoroethylene through mechanical activation, Propell. Explos. Pyrot. 38 (2013) 286–295.
[14] H. Wang, M. Rehwoldt, D.J. Kline, T. Wu, P. Wang, M.R. Zachariah, Comparison study of the ignition and combustion characteristics of directly-written Al/PVDF, Al/Viton and Al/THV composites, Combust. Flame 201 (2019) 181–186.
[15] J.B. Delisio, X. Hu, T. Wu, G.C. Egan, G. Young, M.R. Zachariah, Probing the reaction mechanism of Aluminum/Poly(vinylidene fluoride) Composites, J. Phys. Chem. B 120 (2016) 5534–5542.
[16] J. McCollum, M.L. Pantoya, S.T. Iacono, Activating aluminum reactivity with fluoropolymer coatings for improved energetic composite combustion, ACS Appl. Mater. Inter. 7 (2015) 18742–18749.
[17] J. McCollum, A.M. Morey, S.T. Iacono, Morphological and combustion study of interface effects in aluminum-poly(vinylidene fluoride) composites, Mater. Design 134 (2017) 64–70.
[18] R.S. Janesheski, L.J. Groven, S.F. Son, Fluoropolymer and aluminum piezoelectric reactives, AIP Conf. Proc. 1426 (2012) 741–744.
[19] S.K. Valluri, M. Schoenitz, E. Dreizin, Fluorine-containing oxidizers for metal fuels in energetic formulations, Def. Technol. 15 (2019) 1–22.
[20] V. Cauda, S. Stassi, K. Bejtka, G. Canavese, Nanoconfinement: an effective way to enhance PVDF piezoelectric properties, ACS Appl. Mater. Inter. 5 (2013) 6430–6437.
[21] A. Vinogradov, F. Holloway, Electro-mechanical properties of the piezoelectric polymer PVDF, Ferroelectrics 226 (1999) 169–181.
[22] M.G. Broadhurst, G.T. Davis, Physical basis for piezoelectricity in pvdf, Ferroelectrics 60 (1984) 3–13.
[23] X. Cai, T. Lei, D. Sun, L. Lin, A critical analysis of the α, β and γ phases in poly(vinylidene fluoride) using FTIR, RSC Adv 7 (2017) 15382–15389.
[24] L. Ruan, X. Yao, Y. Chang, L. Zhou, G. Qin, X. Zhang, Properties and applications of the β phase poly(vinylidene fluoride), Polymers (Basel) 10 (2018) 228.
[25] E. Fukada, History and recent progress in piezoelectric polymers, IEEE T. Ultrason. Ferr. 47 (2000) 1277–1290.
[26] P. Martins, A.C. Lopes, S. Lanceros-Mendez, Electroactive phases of poly(vinylidene fluoride): determination, processing and applications, Prog. Polym. Sci. 39 (2014) 683–706.
[27] S. Huang, S. Hong, Y. Su, Y. Jiang, S. Fukushima, T.M. Gill, N.E.D. Yilmaz, S. Tiwari, K. ichi Nomura, R.K. Kalia, A. Nakano, F. Shimojo, P. Vashishta, M. Chen, X. Zheng, Enhancing combustion performance of nano-Al/PVDF composites with β-PVDF, Combust. Flame 219 (2020) 467–477.
[28] M. Margevicius, Sensitizing Energetic Materials Using Piezoelectricity (Master's Thesis), Pennsylvania State University, State College, PA, USA, 2019.
[29] T. Sharma, S.S. Je, B. Gill, J.X.J. Zhang, Patterning piezoelectric thin film PVDF-TrFE based pressure sensor for catheter application, Sens. Actuator A Phys. 177 (2012) 87–92.
[30] Y. Li, C. Liao, S.C. Tjong, Electrospun polyvinylidene fluoride-based fibrous scaffolds with piezoelectric characteristics for bone and neural tissue engineering, Nanomaterials 9 (2019) 952.
[31] F.N. Meyers, K.J. Loh, J.S. Dodds, Piezoelectric Characterization of PVDF-TrFE Thin Films Enhanced With ZnO Nanoparticles, IEEE Sens. J. 12 (2012) 1889–1890.
[32] J. Han, D. Li, C. Zhao, X. Wang, J. Li, X. Wu, Highly sensitive impact sensor based on PVDF-TrFE/Nano-ZnO composite thin film, Sensors 19 (2019) 830.
[33] L. Shu, R. Liang, Z. Rao, L. Fei, S. Ke, Y. Wang, Flexoelectric materials and their related applications: a focused review, J. Adv. Ceram. 8 (2019) 153–173.
[34] D. Skinner, D. Olson, A. Block-Bolten, Electrostatic discharge ignition of energetic materials, Propell. Explos. Pyrot. 23 (1998) 34–42.
[35] Z. Wang, R. Song, Z. Shen, W. Huang, C. Li, S. Ke, L. Shu, Non-linear behavior of flexoelectricity, Appl. Phys. Lett. 115 (2019) 252905.
[36] S. Baskaran, N. Ramachandran, X. He, S. Thiruvannamalai, H.J. Lee, H. Heo, Q. Chen, J.Y. Fu, Giant flexoelectricity in polyvinylidene fluoride films, Phys. Lett. A 375 (2011) 2082–2084.
[37] J. Liu, Y. Zhou, X. Hu, B. Chu, Flexoelectric effect in PVDF-based copolymers and terpolymers, Appl. Phys. Lett. 112 (2018) 232901.
[38] B. Chu, D.R. Salem, Flexoelectricity in several thermoplastic and thermosetting polymers, Appl. Phys. Lett. 101 (2012) 103905.
[39] S. Poddar, S. Ducharme, Measurement of the flexoelectric response in ferroelectric and relaxor polymer thin films, Appl. Phys. Lett. 103 (2013) 202901.
[40] R.K. Walzel, V.I. Levitas, M.L. Pantoya, Aluminum particle reactivity as a function of alumina shell structure: amorphous versus crystalline, Powder Technol 374 (2020) 33–39.
[41] R. Thiruvengadathan, Aluminum-based nano-energetic materials: state of the art and future perspectives, in: S. Bhattacharya, A. Agarwal, T. Rajagopalan, V. Patel (Eds.), Nano-Energetic Materials, Eds., Springer, Singapore (2019), pp. 9–35.
[42] K.W. Watson, M.L. Pantoya, V.I. Levitas, Fast reactions with nano- and micrometer aluminum: a study on oxidation versus fluorination, Combust. Flame 155 (2008) 619–634.
[43] S.L. Row, L.J. Groven, Smart energetics : sensitization of the aluminum-fluoropolymer reactive system, 20 (2018) 1700409.
[44] K.E. Uhlenhake, D. Olsen, M. Gomez, M. Örnek, M. Zhou, S.F. Son, Photoflash and laser ignition of full density nano-aluminum PVDF films, Combust. Flame 233 (2021) 111570.
[45] B.S. Ince-Gunduz, R. Alpern, D. Amare, J. Crawford, B. Dolan, S. Jones, R. Kobylarz, M. Reveley, P. Cebe, Impact of nanosilicates on poly(vinylidene fluoride) crystal polymorphism: part 1. Melt-crystallization at high supercooling, Polymer (Guildf) 51 (2010) 1485–1493.
[46] A. Salimi, A.A. Yousefi, FTIR studies of β-phase crystal formation in stretched PVDF films, Polym. Test. 22 (2003) 699–704.
[47] E. Ghafari, X. Jiang, N. Lu, Surface morphology and beta-phase formation of single polyvinylidene fluoride (PVDF) composite nanofibers, Adv. Compos. Hybrid Mater. 1 (2018) 332–340.
[48] B.T. Neyer, A D-optimality-based sensitivity test, Technometrics 36 (1994) 61–70.
[49] J.H. (Jay) Shin, M. Zhou, Piezoelectric response of energetic composites under an electrostatic excitation, J. Appl. Phys. 129 (2021) 245103.
[50] H. Chalal, F. Abed-Meraim, Hardening effects on strain localization predictions in porous ductile materials using the bifurcation approach, Mech. Mater. 91 (2015) 152–166.
[51] J.T. Mang, R.P. Hjelm, S.F. Son, P.D. Peterson, B.S. Jorgensen, Characterization of components of nano-energetics by small-angle scattering techniques, J. Mater. Res. 22 (2007) 1907–1920.
[52] J.Y. Bottero, D. Tchoubar, J.M. Cases, F. Fiessinger, Investigation of the hydrolysis of aqueous solutions of aluminum chloride. 2. Nature and structure by small-angle X-ray scattering, J. Phys. Chem. 86 (1982) 3667–3673.